• RESEARCH PAPER •

Efficient charge transfer in $WS_2/W_xMo_{1-x}S_2$ heterostructure empowered by energy level hybridization

Xuhong AN[1†], Yehui ZHANG[1†], Yuanfang YU[1], Weiwei ZHAO[1], Yutian YANG[1], Xianghong NIU[3], Xuan LUO[2], Junpeng LU[1*], Jinlan WANG[1*] & Zhenhua NI[1*]

[1]*School of Physics and Key Laboratory of MESMS of the Ministry of Education, Southeast University, Nanjing 211189, China;*
[2]*Key Laboratory of Materials Physics, Institute of Solid State Physics, Chinese Academy of Sciences, Hefei 230031, China;*
[3]*New Energy Technology Engineering Laboratory of Jiangsu Province and School of Science, Nanjing University of Posts and Telecommunications, Nanjing 210023, China*

Abstract Photoinduced charge transfer (CT) is decisive to the efficiency and speed of photoelectric conversion in two-dimensional (2D) van der Waals (vdWs) heterostructures. Generally, CT rate enhancement is realized by increasing the band offset (BO). In this study, we propose that a fast and efficient CT can be realized via strong hybridization of energy levels in 2D vdWs heterostructures with minimal BO. First-principles calculations reveal that the smallest energy difference between conduction-band edges and minimal BO in the $WS_2/W_xMo_{1-x}S_2$ ($x = 0.78$) heterostructure yields the strong hybridization of energy levels and then results in ultrafast CT (2.7 ps). Experimental results agree with theoretical calculations. The photoluminescence of WS_2 is quenched in the $WS_2/W_xMo_{1-x}S_2$ ($x = 0.78$) heterostructure, attributable to the strong hybridization-induced fast and efficient CT. This study provides insights into the mechanism of CT in heterostructures and offers new strategies to create superior optoelectronic devices with fast and efficient photoelectric conversion.

Keywords van der Waals heterostructure, band offset, hybridization strength, charge transfer, photoluminescence quenching

1 Introduction

Charge transfer (CT) is an essential basis of functional electronic and optoelectronic devices [1–7]. Increasing the CT rate (CTR) is a crucial strategy to realize high-speed and efficient optoelectronic devices, such as photodetectors, photocatalysis, and solar cells. In heterostructures, the CTR is generally enhanced by a significant driving force, i.e., the band offset (BO) between two materials [8]. However, additional energy loss would be induced by a large BO, which would limit the maximum achievable efficiency of photoelectric conversion [9, 10]. Another key approach to enhance the CTR is increasing the electronic coupling strength at the heterointerface, which can be controlled by various means, such as interfacial quality, stacking geometry, and hybridization of energy levels [11–13]. The energy level hybridization strength is proportional to the overlap of wavefunctions between two materials, which occurs only at the scale of atomic radius [14]. Therefore, the hybridization strength is strongly influenced by dimensionality. For bulk heterostructures, the width of a depletion region where photoelectric conversion occurs is approximately hundreds of nanometers [15, 16], and the effect of the hybridization of energy levels is

negligible. When the dimensionality decreases from three-dimensional (3D) to 2D, strong hybridization of energy levels could be achieved because the width of the depletion region is exactly the thickness of the junction in 2D van der Waals (vdWs) vertical heterostructures [17]. Therefore, constructing a 2D vdWs heterostructure might be a facile and straightforward method to realize fast and efficient CT. This heterostructure requires strong interfacial coupling empowered by the hybridization of energy levels under the minimal BO condition.

In this study, we built a model of the $WS_2/W_xMo_{1-x}S_2$ heterostructure in which continuous BO and hybridization strength could be provided by controlling the chemical composition (x) of the ternary alloy. Through theoretical simulation and experimental verification, we demonstrated that the hybridization of energy levels strongly affected the CTR, especially under the minimal BO condition. A CT time of 2.7 ps was achieved for $x = 0.78$, which was due to the interplay between the interlayer coupling caused by the hybridization of energy levels and BO. This was further verified by experiments in which the photoluminescence (PL) of WS_2 was quenched in the $WS_2/W_xMo_{1-x}S_2$ ($x = 0.78$) heterostructure.

2 Results

Figure 1(a) illustrates the band structure of a heterostructure with type-II band alignment. The CTR in this heterostructure was strongly influenced by the BO between two materials, i.e., the driving force for separating the photoexcited electron-hole pairs. Further, the CTR was highly dependent on electronic coupling strength (V_{DA}), which was caused by the hybridization of energy levels between two materials, denoted by hybridization strength (Figures 1(a) and (b)). The coupling strength can be evaluated using a diabatic-state approach:

$$V_{DA} = \langle \psi^D | H | \psi^A \rangle, \tag{1}$$

where ψ^D and ψ^A are the wavefunctions of the initial and final states, respectively and H is the interaction potential [18, 19]. Considering electron transfer as an example, with a decrease in conduction BO, energy levels involving CT between two materials become closer, and their hybridization becomes stronger. This enables greater penetration of the electron wavefunctions from one material (M1) into another (M2); therefore, the transition matrix elements (TMEs) between the two states are increased. The CTR k_{ct} dependence on the BO and hybridization strength can be described by classical Marcus theory as follows [20, 21]:

$$k_{ct} = \sqrt{\frac{4\pi^3}{h^2 \lambda k_B T}} |V_{DA}|^2 \exp -\frac{(\Delta G_0 + \lambda)^2}{4\lambda k_B T}, \tag{2}$$

where h is the Planck constant, k_B is the Boltzmann constant, T is the temperature, V_{DA} is the hybridization strength, ΔG_0 is the free energy (BO), and λ is the reorganization energy derived from the variations in bond length and angle, which is very small due to the similar crystal structures of WS_2 and MoS_2. Besides, the CTR depends on the activation energy ($\Delta G^{\neq}$) and is described as follows:

$$k_{ct} = \sqrt{\frac{4\pi^3}{h^2 \lambda k_B T}} |V_{DA}|^2 \exp -\frac{\Delta G^{\neq}}{k_B T}, \tag{3}$$

where the activation energy ($\Delta G^{\neq}$) is given by

$$\Delta G^{\neq} = \frac{(\Delta G_0 + \lambda)^2}{4\lambda}. \tag{4}$$

From (4), $\Delta G^{\neq}$ is a quadratic function of ΔG_0; k_{ct} is a negative exponential function of $\Delta G^{\neq}$, shown by (3). When $-\Delta G_0 > \lambda$, $\Delta G^{\neq}$ decreases, and k_{ct} increases with an increase in ΔG_0; when $-\Delta G_0 < \lambda$, $\Delta G^{\neq}$ increases, the reaction is in the Marcus inverted region. In addition, k_{ct} decreases with an increase in ΔG_0. In our heterostructure, ΔG_0 is larger than λ, so the rate is facilitated by a large BO. In this case, the hybridization of the energy level is very weak in the heterostructure, and a large BO dominates the CT. By contrast, the hybridization strength could also dominate CT and facilitate an extremely high CTR at the status of a small BO (Figure 1(b)). However, for bulk heterostructures, achieving strong electronic coupling by hybridization of energy levels is difficult. This is because wavefunctions overlap only occurs within atomic scales (Figure 1(c)), which is almost negligible compared to the width of the
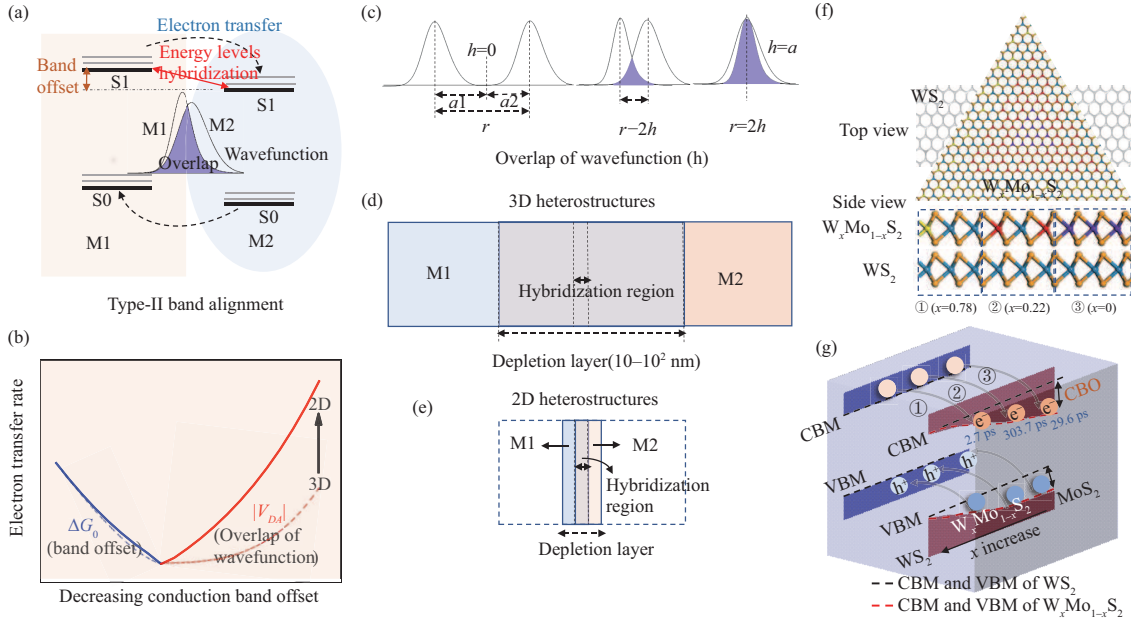
Figure 1 (Color online) Illustration of the hybridization-induced CT. (a) Schematic of CT in the heterostructure with type-II band alignment. (b) CTR depends on BO and hybridization strength (V_{DA}) caused by the hybridization of energy levels; solid depicts 2D heterostructures, whereas dash depicts 3D heterostructures. (c)–(e) The wavefunction overlap (h) depends on the distance (r) between M1 and M2 atoms. The atomic radius of M1 (M2) is donated as $a1$ ($a2$). (c) Schematic of the dependence of overlap on distance. (d) The hybridization of 3D heterostructures. (e) The hybridization of 2D vdWs heterostructures. (f) Schematic of the $WS_2/W_xMo_{1-x}S_2$ heterostructure. (g) CT process in the $WS_2/W_xMo_{1-x}S_2$ heterostructure. ①, ②, ③ presents W composition of $x = 0.78$, 0.22, and 0, respectively.

depletion region where photoelectric conversion occurs (Figure 1(d)). Compared with bulk heterostructures, 2D vdWs heterostructures possess prominent merits, such as atomically thin thickness, no dangling bonds, and unconstrained lattice matches. This implies that strong hybridization of energy levels could be readily achieved and occurs in the entire heterojunction region, as the hybridization region is almost the same as the thicknesses of the materials (Figure 1(e)). WS_2 monolayer and ternary $W_xMo_{1-x}S_2$ monolayer were employed to construct a 2D vdWs heterostructure (Figure 1(f)), and it possessed continuously tunable electronic band structures with changing stoichiometry of W (x) atom, indicating the possibility of realizing energy level hybridization and maximizing the electronic coupling strength. In addition, continuously tunable x could also provide continuously tunable BO [22–27]. Therefore, the $WS_2/W_xMo_{1-x}S_2$ heterostructure is an ideal platform to investigate the CT process under controllable BO and hybridization strength (Figure 1(g)).

Time-dependent ab initio nonadiabatic molecular dynamics (NAMD) was performed to analyze the dependence of CTT on BO and hybridization strength in the $WS_2/W_xMo_{1-x}S_2$ heterostructure. Investigations were focused respectively on five stoichiometric compositions of $x = 1$, 0.78, 0.45, 0.22, and 0. Their band structures are shown in Figures 2(a)–(c) ($x = 0.78$, 0.45 and 0.22) and Figures S1(a) and (b) ($x = 0$ and 1), respectively. The conduction BOs between WS_2 and $W_xMo_{1-x}S_2$ for $x = 0$, 0.22, 0.45, 0.78, and 1 are 357, 341, 292, 152 and 0 meV, respectively. The value of 357 meV in the WS_2/MoS_2 heterostructure agrees with a previous report [28]. The valence band maximum (VBM) does not vary with the change in x because it results from the d_{x2-y2} and d_{xy} orbitals of Mo/W and the p_x and p_y orbitals of S. These orbitals are in-plane interactions and insensitive to the interplay between layers [29]. The conduction-band minimum (CBM) originates from the d_z^2 orbital of Mo/W and the p_x and p_y orbitals of S, which are out-plane interactions that strongly depend on the interplay between layers. For $W_xMo_{1-x}S_2$, the energy difference between the W atom (5d) and Mo atom (4d) facilitates energy level splitting to form Levels 1 and 2. The energy level marked in red (denoted as Level 3) is degenerated and arisen from WS_2. With a decrease in BO (increase in x), Level 3 (WS_2) and Level 2 ($W_xMo_{1-x}S_2$) become closer, and they are nearly degenerated at $x = 0.78$. Meanwhile, the energy difference between Levels 1 and 3 is the smallest. Therefore, a strong hybridization of energy levels occurs, which increases the TMEs and lowers the activation energy based on Henry-Taube theory [30–32]. This facilitates a higher CTR based on the Marcus theory, evidenced by the variations in CTT of 303.7, 27.3, and 2.7 ps
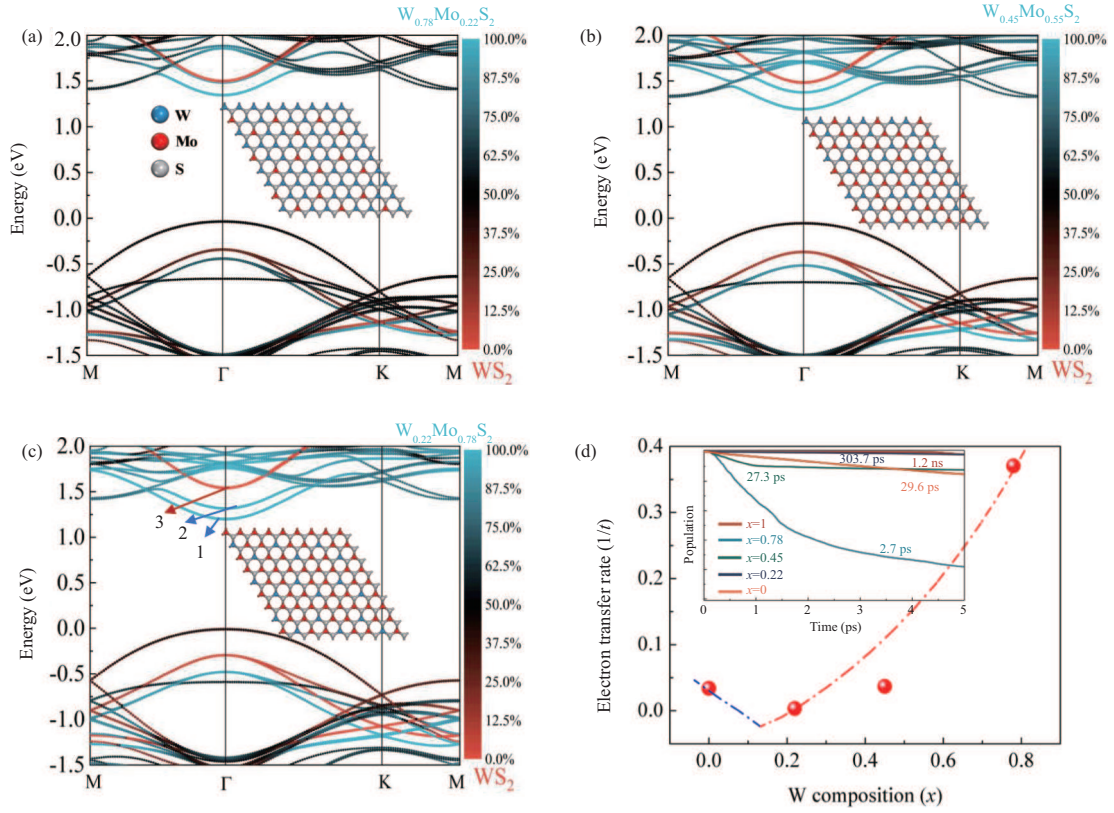
Figure 2 (Color online) Calculated band structures and CTRs of the $WS_2/W_xMo_{1-x}S_2$ heterostructure. (a)–(c) Band structures of $WS_2/W_xMo_{1-x}S_2$ with $x = 0.78$, 0.45, and 0.22, respectively. The energy levels involving CT are mainly red (Level 3) derived from WS_2 and blue energy (Level 1/2) resulting from $W_xMo_{1-x}S_2$. The inserts are the top views of calculation models. (d) CTR ($1/t$) as a function of W composition (x). The CTT are 29.6, 303.7, 27.3, 2.7, and 1200 ps in the $WS_2/W_xMo_{1-x}S_2$ heterostructure with W compositions of $x = 0$, 0.22, 0.45, 0.78, and 1, respectively, as indicated in the inset.

corresponding to $x = 0.22$, 0.45, and 0.78, respectively (Figure 2(d)). Although the energy levels (Levels 1/2 and 3) completely degenerate at $x = 1$, a BO of 0 meV does not satisfy the CT requirement, i.e., back electron transfer would also occur. Consequently, the CTR is very slow (1.2 ns). In the case of $x = 0$ with a BO of 357 meV, the distance between Levels 3 and 1/2 is very large, and the hybridization strength is weak. Therefore, a CTT of 29.6 ps is obtained, wherein this CT process is dominated by the driving force, i.e., the BO.

To further confirm the above result, the time evolutions of the energy level vibrations located at the point at $x = 0.78$, 0.45, and 0.22 were calculated and shown in Figures 3(a)–(c). Levels 1 and 2 in $W_xMo_{1-x}S_2$ and degenerated Level 3 in WS_2 are highlighted. With increasing x from 0.22 to 0.78, the BO decreases from 341 to 152 meV, respectively; i.e., the energy differences between the three energy levels decrease, which leads to stronger vibration and then enables greater penetration of the electron wavefunctions from WS_2 into $W_xMo_{1-x}S_2$ in the heterostructure. Therefore, it increases the TME, lowers the activation energy, and promotes CT. The hybridization strength is quantitatively identified by the nonadiabatic TMEs. As shown in Figures 3(d)–(f), the coupling between Levels 1 and 2 in $W_xMo_{1-x}S_2$ and degenerated Level 3 in WS_2 at the point forms six TMEs. The nonadiabatic TMEs are 0.095, 0.004, and 0.00093 meV for $x = 0.78$, 0.45, and 0.22, respectively. These are in accordance with the calculated CTTs, which are 2.7, 27.3, and 303.7 ps, respectively.

To experimentally prove the theoretical prediction, the evolution of the CTR in the $WS_2/W_xMo_{1-x}S_2$ heterostructure is probed by means of PL quenching. Generally, the occurrence of CT would induce quenching of PL in type-II heterojunctions. Based on the Stern-Volmer equation, the relationship between the CTR and the degree of PL quenching can be described as follows [33–36]:

$$\frac{1}{\tau_{ct}} \sim \frac{1}{\tau_0} \cdot \frac{I_0}{I}, \tag{5}$$

where $\frac{1}{\tau_0}$ is the radiative decay rate (τ_0 is the lifetime of bare WS_2, which is constant in our system),
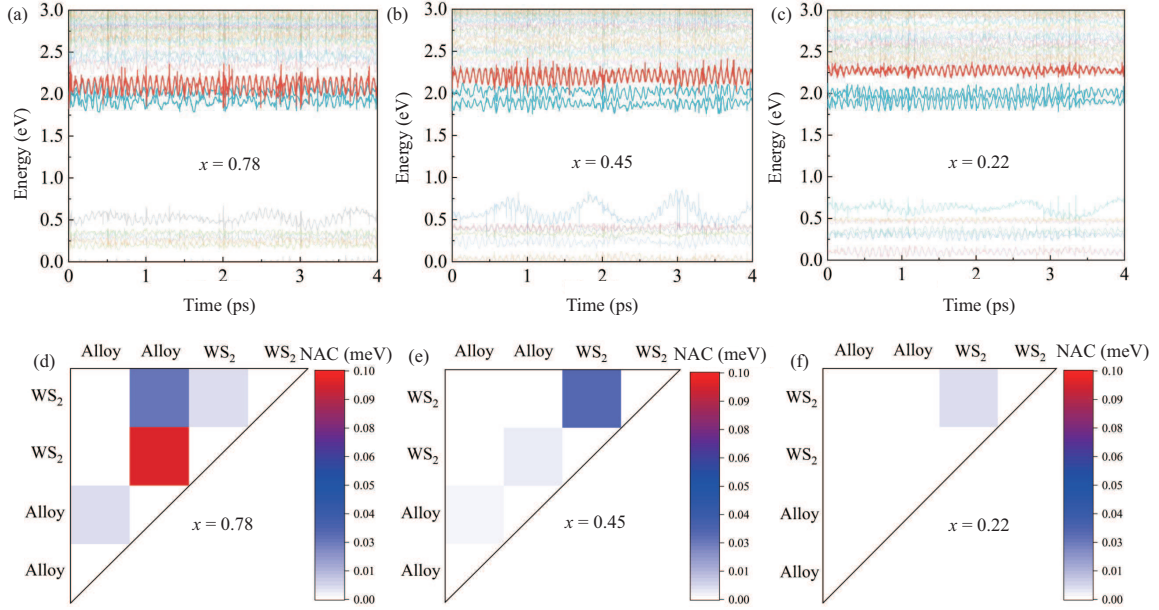
Figure 3 (Color online) The vibration and coupling of energy levels. (a)–(c) Time evolutions of the energy level vibration located at the Γ point (three energy levels involving CT in $W_xMo_{1-x}S_2$ and WS_2 are highlighted) at $x = 0.78$, 0.45, and 0.22. (d) and (f) Nonadiabatic TMEs between energy levels (Levels 1, 2, and 3) at the high symmetry Γ point, corresponding to $x = 0.78$, 0.45, and 0.22, respectively.

and $\frac{I_0}{I}$ is the degree of PL intensity quenching. I_0 is the initial intensity, and I is the PL intensity after quenching. Therefore, the degree of PL quenching is a clear sign of the CTR in heterostructures.

The Raman images of the $WS_2/W_xMo_{1-x}S_2$ heterostructure are shown in Figures S4(a)–(d), which confirms the formation of a heterostructure comprising WS_2 and $W_xMo_{1-x}S_2$ with continuously varying x. Figures 4(a) and (b) depict the PL images of $W_xMo_{1-x}S_2$ centered at 650 nm and WS_2 at 620 nm, respectively. The PL spectra of bare WS_2, bare $W_xMo_{1-x}S_2$ ($x = 0.78$, 0.42, and 0.29), and $WS_2/W_xMo_{1-x}S_2$ heterostructures are shown in Figures 4(c)–(e). Evidently, the intensities of both PL peaks are quenched with the formation of a heterostructure. The quenching degree of the PL intensity of WS_2 presents a significant dependence on the composition (x) variation of $W_xMo_{1-x}S_2$. In particular, the PL intensities of WS_2 are completely quenched when it is stacked on $W_xMo_{1-x}S_2$ with $0.7 < x < 1$ (blue dotted frame in Figures 4(b) and (c)). More results for different samples are shown in Figures S4(e)–(h), and a similar quenching phenomenon is observed. Complete quenching is also observed at a low temperature of 10 K (Figures S5(a) and (b)), demonstrating that quenching arises from CT rather than phonon assistance. Moreover, the peak of WS_2 still exists at $0 < x < 0.7$ (Figures 4(d) and (e)), and the PL intensities are reduced only by two to four times.

Comparison investigations were performed on WS_2/WS_2 (i.e., $x = 1$) and WS_2/MoS_2 (i.e., $x = 0$) heterostructures (Figure S6). The PL intensity of WS_2 was quenched approximately six times in WS_2/WS_2 due to CT, back electron transfer, and stacking order [37]. Moreover, it was up to approximately 21 times higher in the WS_2/MoS_2 heterostructure, which agrees with a previous report [38]. The degree of PL quenching (I_0/I) as a function of W composition (x) is plotted in Figure 5. Considering the synergy of BO and hybridization, the CTR decreases at the initial stage ($0 \leqslant x < 0.2$) with an increase in x due to decreasing BO. In the second stage ($0.2 < x < 0.7$), the hybridization of energy levels plays a more crucial role, and the CTR slightly increases with an increase in x. In the resonant regime ($0.7 < x < 1$), the hybridization of energy levels becomes the dominant factor of CT and facilitates the maximum CTR. This result agrees with the theoretical prediction (Figure 1(b)).

3 Summary

In summary, we demonstrated that fast and efficient CT with minimal BO could be realized by strong hybridization of energy levels in 2D vdWs heterostructures. Our computational results in the $WS_2/W_xMo_{1-x}S_2$ heterostructure showed that a low BO yielded strong hybridization between the energy
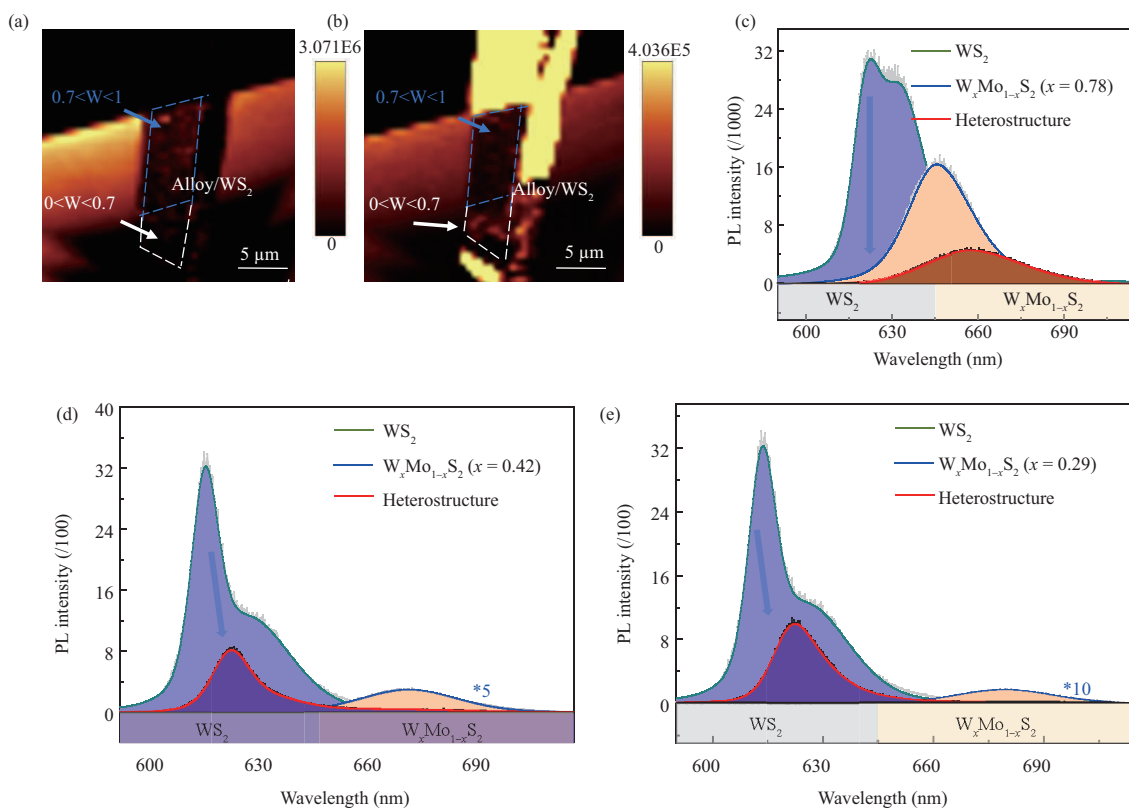
Figure 4 (Color online) PL mappings and spectra of WS_2, $W_xMo_{1-x}S_2$, and $WS_2/W_xMo_{1-x}S_2$ heterostructure. (a) PL image of $W_xMo_{1-x}S_2$ peak at $\sim$650 nm. (b) PL image of WS_2 peak at $\sim$620 nm. (c)–(e) PL spectra and fitted results of bare WS_2, bare $W_xMo_{1-x}S_2$, and $WS_2/W_xMo_{1-x}S_2$ at $x = 0.78$, 0.42, and 0.29, respectively.
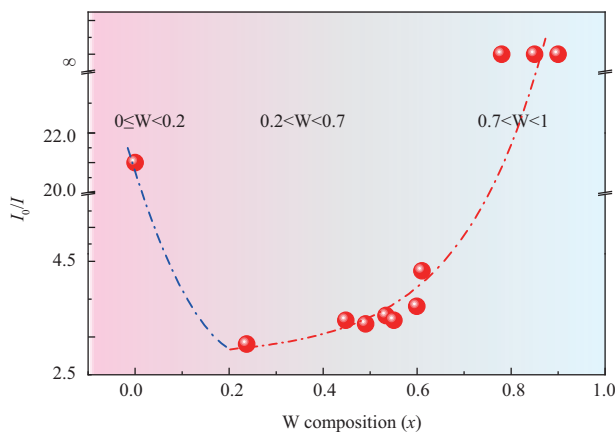
Figure 5 (Color online) The degree of PL quenching (I_0/I) of WS_2 as a function of W composition. I_0 is the initial intensity, and I is the intensity after quenching.

levels in bare WS_2 and $W_xMo_{1-x}S_2$, attributable to the closer energy and stronger vibration of energy levels involved in CT. The CTT of 2.7 ps was achieved at $x = 0.78$, and it was even faster at $0.78 < x < 1$. These results agree with the experimental results of the completely quenched PL of WS_2 in the heterostructure region of $WS_2/W_xMo_{1-x}S_2$ ($x = 0.78$). Understanding the dependence of the CTR on the BO, interlayer coupling strength caused by the hybridization of energy levels, and the degree of PL quenching is beneficial for the fabricating of high-performance electronic and optoelectronic devices based on the vdWs heterostructures.

Experimental and calculational methods.

Synthesis: $W_xMo_{1-x}S_2$ monolayers were grown on SiO_2/Si (300-nm oxide layer) substrates via a two-step chemical vapor deposition approach under atmospheric pressure. The synthesis was performed in a

tube furnace with dual-heating zones. A quartz boat containing sulfur powder (99.5%) was positioned in the first heating zone, whereas another boat containing MoO_3 (99.99%) or WO_3 (99.99%) powder was placed in the second heating zone (Figure S1(a)). The substrate was positioned on top of the boat containing MoO_3 (WO_3) and faced down. A tube chamber was pumped to 10 Pa, and then, argon gas (99.99%) was introduced into the chamber as the carrier gas. The system ramped to temperatures of 220°C for S powders and 700°C for MoO_3 ($WO_3 \sim 1075$ °C) for the first and second zones, respectively. The temperature was maintained for ~ 10 min and then cooled naturally.

Heterostructure fabrication: The WS_2 monolayer was transferred onto $W_xMo_{1-x}S_2$ via the standard dry transfer method under room temperature and air [39]. First, a WS_2 monolayer was exfoliated onto a polydimethylsiloxane film from a bulk crystal under room temperature and air and then transferred onto a $W_xMo_{1-x}S_2$ monolayer using an optical microscope with an aligned transfer system.

PL and Raman characterizations: Raman and PL images and spectra were collected using a WITec alpha300R confocal system under room temperature and air. A 532 nm laser was employed to excite the samples. The laser power was controlled at < 0.5 mW to avoid laser-induced heating. The spot size of the laser beam was ~ 1 μm after focusing.

Computational details: Geometric optimization and electric structure calculations were performed based on density functional theory (DFT), implemented in the Vienna ab initio simulation package code. The Perdew-Burke-Ernzerhof functional of the generalized gradient approximation was chosen as the exchange-correlation function, and the projected augmented wave method was used. A vacuum region of 15 Å was used to prevent the interaction between two adjacent layers. In addition, the energy of 10^{-5} eV and the force of 0.02 eV $\cdot$ Å^{-1} are considered the convergence criteria. During geometry optimization and electronic structure calculation, cutoff energy of 500 eV and k-point meshes of $9 \times 9 \times 1$ were set. The vdW interactions resulting from the long-range effect are added with the DFT-D3 method of Grimme.

NAMD calculations were performed using the PYXAID code, which simulates photoexcited carrier relaxation using the decoherence-induced surface hopping method in time-dependent DFT in the Kohn-Sham model. The adiabatic molecular dynamics (MD) was first performed to execute NAMD calculations. A total of 54 atoms were used to construct a 3×3 hexagonal supercell including a heterostructure. Every structure was completely relaxed at 0 K, then heated to 300 K, and held on 10 ps by repeated velocity rescaling. Afterward, an 8 ps adiabatic MD orbit was acquired in the microcanonical ensemble (NVE) with a 1 fs nuclear time step, and the nonadiabatic coupling matrix elements were simulated along the orbit. A total of 400 geometries were considered as the original configurations for evaluating the electron dynamics during the first 2 ps MD trajectory. Five ps NAMD emulations were executed for various models.

Supporting information Appendix A. The supporting information is available online at info.scichina.com and link.springer.com. The supporting materials are published as submitted, without typesetting or editing. The responsibility for scientific accuracy and content remains entirely with the authors.

References

1 Deng Y, Luo Z, Conrad N J, et al. Black phosphorus-monolayer MoS_2 van der Waals heterojunction p-n diode. ACS Nano, 2014, 8: 8292–8299

2 Liu X, Wang W H, Yang F, et al. Bi_2O_2Se/BP van der Waals heterojunction for high performance broadband photodetector. Sci China Inf Sci, 2021, 64: 140404

3 Gong F, Luo W, Wang J, et al. High-sensitivity floating-gate phototransistors based on WS_2 and MoS_2. Adv Funct Mater, 2016, 26: 6084–6090

4 Lee I, Rathi S, Lim D, et al. Gate-tunable hole and electron carrier transport in atomically thin dual-channel WSe_2/MoS_2 heterostructure for ambipolar field-effect transistors. Adv Mater, 2016, 28: 9519–9525

5 Lee K H, Kim T H, Shin H J, et al. Highly efficient photocurrent generation from nanocrystalline graphene-molybdenum disulfide lateral interfaces. Adv Mater, 2016, 28: 1793–1798

6 Roy T, Tosun M, Cao X, et al. Dual-Gated MoS_2/WSe_2 van der Waals tunnel diodes and transistors. ACS Nano, 2015, 9: 2071–2079

7 Zhang K, Zhang T, Cheng G, et al. Interlayer transition and infrared photodetection in atomically thin type-II $MoTe_2/MoS_2$ van der Waals heterostructures. ACS Nano, 2016, 10: 3852–3858

8 Bai S, Jiang J, Zhang Q, et al. Steering charge kinetics in photocatalysis: intersection of materials syntheses, characterization techniques and theoretical simulations. Chem Soc Rev, 2015, 44: 2893–2939

9 Liu J, Chen S, Qian D, et al. Fast charge separation in a non-fullerene organic solar cell with a small driving force. Nat Energy, 2016, 1: 16089

10 Eisner F D, Azzouzi M, Fei Z, et al. Hybridization of local exciton and charge-transfer states reduces nonradiative voltage losses in organic solar cells. J Am Chem Soc, 2019, 141: 6362–6374

11 Tongay S, Fan W, Kang J, et al. Tuning interlayer coupling in large-area heterostructures with CVD-grown MoS$_2$ and WS$_2$ monolayers. Nano Lett, 2014, 14: 3185–3190

12 Zhang J, Hong H, Lian C, et al. Interlayer-state-coupling dependent ultrafast charge transfer in MoS$_2$/WS$_2$ bilayers. Adv Sci, 2017, 4: 1700086

13 Alexeev E M, Ruiz-Tijerina D A, Danovich M, et al. Resonantly hybridized excitons in moiré superlattices in van der Waals heterostructures. Nature, 2019, 567: 81–86

14 Sih G C. Electron cloud overlap related to specific energy threshold and breakdown at high temperature, short time and nano distance. Theor Appl Fract Mech, 2008, 50: 173–183

15 Louro P, Vieira M, Vygranenko Y, et al. Transport mechanism in high resistive silicon carbide heterostructures. Appl Surf Sci, 2001, 184: 144–149

16 van Hove M, Pereira R, de Raedt W, et al. Zero-dimensional states in submicron double-barrier heterostructures laterally constricted by hydrogen plasma isolation. J Appl Phys, 1992, 72: 158–160

17 Liu Y, Weiss N O, Duan X, et al. Van der Waals heterostructures and devices. Nat Rev Mater, 2016, 1: 16042

18 Yi Y, Coropceanu V, Brédas J L. A comparative theoretical study of exciton-dissociation and charge-recombination processes in oligothiophene/fullerene and oligothiophene/perylenediimide complexes for organic solar cells. J Mater Chem, 2011, 21: 1479

19 Kawatsu T, Coropceanu V, Ye A, et al. Quantum-chemical approach to electronic coupling: application to charge separation and charge recombination pathways in a model molecular donor-acceptor system for organic solar cells. J Phys Chem C, 2008, 112: 3429–3433

20 Chuang C H, Doane T L, Lo S S, et al. Measuring electron and hole transfer in core/shell nanoheterostructures. ACS Nano, 2011, 5: 6016–6024

21 Scholes G D, Jones M, Kumar S. Energetics of photoinduced electron-transfer reactions decided by quantum confinement. J Phys Chem C, 2007, 111: 13777–13785

22 Komsa H P, Krasheninnikov A V. Two-dimensional transition metal dichalcogenide alloys: stability and electronic properties. J Phys Chem Lett, 2012, 3: 3652–3656

23 Kang J, Tongay S, Li J, et al. Monolayer semiconducting transition metal dichalcogenide alloys: stability and band bowing. J Appl Phys, 2013, 113: 143703

24 Xi J, Zhao T, Wang D, et al. Tunable electronic properties of two-dimensional transition metal dichalcogenide alloys: a first-principles prediction. J Phys Chem Lett, 2013, 5: 285–291

25 Zhang W, Li X, Jiang T, et al. CVD synthesis of Mo$_{(1-x)}$W$_x$S$_2$ and MoS$_{2(1-x)}$Se$_{2x}$ alloy monolayers aimed at tuning the bandgap of molybdenum disulfide. Nanoscale, 2015, 7: 13554–13560

26 Wang Z, Liu P, Ito Y, et al. Chemical vapor deposition of monolayer Mo$_{1-x}$W$_x$S$_2$ crystals with tunable band gaps. Sci Rep, 2016, 6: 21536

27 Liu X, Wu J, Yu W, et al. Monolayer W$_x$Mo$_{1-x}$S$_2$ grown by atmospheric pressure chemical vapor deposition: bandgap engineering and field effect transistors. Adv Funct Mater, 2017, 27: 1606469

28 Gong C, Zhang H, Wang W, et al. Band alignment of two-dimensional transition metal dichalcogenides: application in tunnel field effect transistors. Appl Phys Lett, 2013, 103: 053513

29 Kang J, Tongay S, Zhou J, et al. Band offsets and heterostructures of two-dimensional semiconductors. Appl Phys Lett, 2013, 102: 012111

30 Taube H. Electron transfer between metal complexes—a retrospective view (nobel lecture). Angew Chem Int Ed Engl, 1984, 23: 329–339

31 Sutin N. Theory of electron transfer reactions: insights and hindsights. In: Progress in Inorganic Chemistry: An appreciation of Henry Taube. Hoboken: John Wiley & Sons, Inc., 1983. 441–498

32 Taube H. Electronic coupling mechanisms in mixed-valence molecules. Ann NY Acad Sci, 1978, 313: 481–495

33 Carraway E R, Demas J N, DeGraff B A. Luminescence quenching mechanism for microheterogeneous systems. Anal Chem, 1991, 63: 332–336

34 Sariciftci N S, Smilowitz L, Heeger A J, et al. Photoinduced electron transfer from a conducting polymer to buckminsterfullerene. Science, 1992, 258: 1474–1476

35 Wang J, Wang D, Miller E K, et al. Photoluminescence of water-soluble conjugated polymers: origin of enhanced quenching by charge transfer. Macromolecules, 2000, 33: 5153–5158

36 Merkl J P, Wolter C, Flessau S, et al. Investigations of ion transport through nanoscale polymer membranes by fluorescence quenching of CdSe/CdS quantum dot/quantum rods. Nanoscale, 2016, 8: 7402–7407

37 Ji Z, Hong H, Zhang J, et al. Robust stacking-independent ultrafast charge transfer in MoS$_2$/WS$_2$ bilayers. ACS Nano, 2017, 11: 12020–12026

38 Yu Y, Hu S, Su L, et al. Equally efficient interlayer exciton relaxation and improved absorption in epitaxial and nonepitaxial MoS$_2$/WS$_2$ heterostructures. Nano Lett, 2015, 15: 486–491

39 Yang R, Zheng X, Wang Z, et al. Multilayer MoS$_2$ transistors enabled by a facile dry-transfer technique and thermal annealing. J Vac Sci Technol B, 2014, 32: 061203